Promising photocatalysts with high carrier mobility for water splitting in monolayer Ge2P4S2 and Ge2As4S2

Yun-Lai Zhu, Jun-Hui Yuan, Ya-Qian Song, Kan-Hao Xue, Sheng Wang, Chen Lian, Zhao-Nan Li, Ming Xu, Xiao-Min Cheng, Xiang-Shui Miao

To cite this version:

Yun-Lai Zhu, Jun-Hui Yuan, Ya-Qian Song, Kan-Hao Xue, Sheng Wang, et al.. Promising photocatalysts with high carrier mobility for water splitting in monolayer Ge2P4S2 and Ge2As4S2. International Journal of Hydrogen Energy, 2019, 44, pp.21536 - 21545. 10.1016/j.ijhydene.2019.06.068 . hal-03488247

HAL Id: hal-03488247
https://hal.science/hal-03488247v1

Submitted on 20 Jul 2022

Version of Record: https://www.sciencedirect.com/science/article/pii/S0360319919323110
Manuscript_e4360b471da59e6392207aa396a862a5

Promising photocatalysts with high carrier mobility for water splitting in monolayer $Ge_2P_4S_2$ and $Ge_2As_4S_2$

Yun-Lai Zhu,[a+] Jun-Hui Yuan,[a+] Ya-Qian Song,[a] Kan-Hao Xue,[a,b*] Sheng Wang,[a] Chen Lian,[a] Zhao-Nan Li,[a] Ming Xu,[a] Xiao-Min Cheng,[a*] Xiang-Shui Miao[a]

[a]Wuhan National Research Center for Optoelectronics, School of Optical and Electronic Information, Huazhong University of Science and Technology, Wuhan 430074, China

[b]Univ. Grenoble Alpes, Univ. Savoie Mont Blanc, CNRS, Grenoble INP, IMEP-LAHC, 38000 Grenoble, France

[+]The authors Y.-L. Zhu and J.-H. Yuan contributed equally to this work.

Corresponding Authors

*E-mail: xmcheng@hust.edu.cn (X.-M. Cheng) xkh@hust.edu.cn (K.-H. Xue)

Abstract

Monolayer $Ge_2P_4S_2$ and $Ge_2As_4S_2$ are proposed as a new type of efficient photocatalyst for water splitting, based on first-principles calculations. Monolayer $Ge_2As_4S_2$ exhibits a direct band gap of 1.89 eV (based on HSE06 calculation), while monolayer $Ge_2P_4S_2$ is an indirect gap semiconductor that can turn into direct band gap by applying 3% compressive strain. Moreover, the band edge positions of monolayer $Ge_2P_4S_2$ and $Ge_2As_4S_2$ perfectly cover the redox potentials of water. Remarkably, the $Ge_2P_4S_2$ and $Ge_2As_4S_2$ monolayers possess rather high carrier mobilities (~10^3-10^4 cm^2 V^{-1} s^{-1}), and have moderate optical absorption performance in the range of visible light. In addition, the adsorption and decomposition of water molecules on monolayer $Ge_2P_4S_2$ and $Ge_2As_4S_2$ are explored to illustrate the mechanism of photocatalytic hydrogen formation. These results demonstrate that the monolayer $Ge_2P_4S_2$ and $Ge_2As_4S_2$ hold great potential for photocatalytic water splitting.

Keywords:

2D Materials; Photocatalysts; Direct band gap; Carrier mobility; Water splitting

1. Introduction

Photocatalytic water splitting to produce hydrogen and oxygen has been considered as a potential means for resolving the serious energy and environment problems [1–6]. Thus far, enormous works have been performed since the discovery of TiO_2 as an effective photocatalyst for water splitting [7–15]. A primary requirement for such photocatalyst is that the conduction band minimum (CBM) should stay above the hydrogen reduction potential (H^+/H_2), while the valence band maximum (VBM) should lie below the water oxidation potential (H_2O/O_2) [16,17]. Consequently, its band gap must be larger than the 1.23 eV threshold, but nevertheless lower than 3.00 eV for the purpose of efficient solar energy harvesting [18,19]. Therefore, an intermediate band gap around 1.8 eV is considered ideal for visible-light photocatalytic water splitting [20–23].

Two-dimensional (2D) materials have been extensively investigated for photocatalytic water splitting, due to their distinct properties such as high specific surface areas, high photon-harvesting efficiency in the visible light region, and small charge transport distances [18,24–26]. All these reduce the probability of electron-hole recombination, bringing about enhanced photocatalytic performance. For example, monolayer ZnSe exhibits a great photocurrent density up to 2.14 mA cm^{-2}, which is about 195 times higher than that of its bulk [27]. Besides, plenty of 2D materials have been synthesized experimentally or predicated theoretically for photocatalyst application, such as transition metal dichalcogenides [28], g-C_3N_4 [29–31], group-III mono-chalcogenides [32], and so forth. However, achieving both fast carrier migration and effective separation of photo-generated electrons and holes in these 2D materials remains challenging.

Recently, Jing *et al.* proposed 2D GeP_3 with the buckling blue phosphorene-type honeycomb structure, showing strong interlayer quantum confinement and high carrier mobility up to 8.84×10^3 cm^2 V^{-1} s^{-1} for the bilayer [33]. Thereafter, a series of monolayer metal phosphides such as GaP_3 [34], InP_3 [35], SnP_3 [36] and TlP_5 [37], with high carrier mobilities have been theoretically predicted, which are candidates for optoelectronic applications. However, these 2D materials are not suitable for photocatalytic water splitting, because of their small band gap values or improper CBM/VBM positions. For example, monolayer SnP_3 only has an indirect band gap of 0.83 eV, albeit possessing very high carrier mobilities in the range of 3000-7000 cm^2 V^{-1} s^{-1} [38]. On the other hand, through proper element substitution, certain ternary compounds can be designed to fulfill the desired electronic properties. Typical examples involve Si_2BN [39], P_2SiS[40] and $BNBe_3$ [41]. Hence, it is expected that the band gap of monolayer GeP_3 can be intentionally adjusted by neighboring elements substitution.

In this work, two isoelectric monolayer compounds based on GeP_3 and $GeAs_3$ are designed, where part of the P/As atoms are replaced by S atoms. The resulting monolayer $Ge_2P_4S_2$ and $Ge_2As_4S_2$ well meet the desired band gap value and band edge positions required by water redox potentials. Through thermodynamic and kinetic stability as well as carrier mobility studies, we shall show the great potential of monolayer $Ge_2P_4S_2$ and $Ge_2As_4S_2$ in photocatalytic water splitting.

2. Computational methods

All calculations were based on density functional theory (DFT) as implemented in the Vienna *Ab initio* Simulation Package (VASP) [42]. The electrons considered as valence were 3d, 4s and 4p for Ge; 3s and 3p for P; 3s and 3p for S; 4s and 4p for As; 2s and 2p for O; 1s for H. Core electrons were replaced by projector augmented-wave (PAW) pseudopotentials [43]. The generalized gradient approximation (GGA) within the Perdew-Burke-Ernzerhof (PBE) functional form [44] was adopted for the exchange-correlation energy. The plane-wave kinetic energy cutoff was fixed to be 500 eV. The geometric structures were fully relaxed with the force convergence criterion set to 0.001 eV $Å^{-1}$, while all self-consistent electronic loops were regarded as convergent when the energy difference between two consecutive steps became less than 10^{-7} eV. A vacuum space of ~20 Å along the z direction was used to minimize the undesired interaction between the atomic layer and its periodic images. The Brillouin zone sampling was carried out using equal spacing Γ-centered 11×11×1 k-point mesh for structural relaxation. The Heyd-Scuseria-Ernzerhof (HSE06) screened exchange hybrid functional [45] was also adopted to characterize the electronic and optical properties more precisely. The phonon dispersion relations were calculated with the density functional perturbation theory as implemented in the PHONOPY code [46,47]. In addition, *ab initio* molecular dynamics (AIMD) simulations were performed to assess the thermodynamic stability of the structures, where canonical ensembles (NVT) were used [48].

3. Results and discussion

3.1 Atomic structures and stability analysis

As shown in **Figs. 1a and 1b**, the optimized structure of $Ge_2P_4S_2$ ($Ge_2As_4S_2$) monolayer is similar to the recently investigated GeP_3 [33], where only two P atoms in the hexagonal unit cell of GeP_3 are replaced by S atoms. Detailed geometric data are further listed in **Table 1**. The optimized lattice constant of $Ge_2P_4S_2$ is 6.77 Å with a buckling height of 1.91 Å, while the lattice constant of $Ge_2As_4S_2$ increases to 7.10 Å, accompanied by a corresponding 1.85 Å buckling height. The visualization of the electron localization function (ELF) [49] is conducted to investigate the nature of the chemical bonding in $Ge_2P_4S_2$ (see **Fig. 1c**). The ELF values of 1, 0.5 and 0 correspond to fully localized electrons, free electron gas and the absence of electrons, respectively. A substantial concentration of electrons is found to reside along the Ge-P and Ge-S bonds, while the difference in the ELF values of various atoms exists, indicating the coexistence of covalent bond and ionic bond for Ge-P and Ge-S. The Bader charge analysis [50] further reveals that in $Ge_2P_4S_2$ the Ge/P atom has lost 0.54/0.02 e, while the S atom has gained 0.57 e; in $Ge_2As_4S_2$ the amount of electron loss is 0.43/0.12 e for the Ge/As atom and the amount of electron gain is 0.66e for the S atom. Subsequently, we calculated the cohesive energy E_C, which is defined by $E_C = -[E_{total} - n_1 E(\mathrm{Ge}) - n_2 E(\mathrm{P/As}) - n_3 E(\mathrm{S})]/(n_1 + n_2 + n_3)$ [51]. Here E_{total} stands for the energy of $Ge_2P_4S_2$ ($Ge_2As_4S_2$) per unit cell, E(Ge), E(P/As), and E(S) are the energies of free Ge, P(As) and S atoms, and n_1, n_2 and n_3 are the numbers of Ge, P(As) and S atoms per unit cell. We find E_C to be 3.40 eV/ atom for $Ge_2P_4S_2$ and 3.15 eV/atom for $Ge_2As_4S_2$, which are comparable with blue phosphorene (3.29 eV/atom) [52]. Hence, it is possible to experimentally synthesize monolayer $Ge_2P_4S_2$ and $Ge_2As_4S_2$ from an energetic point of view.

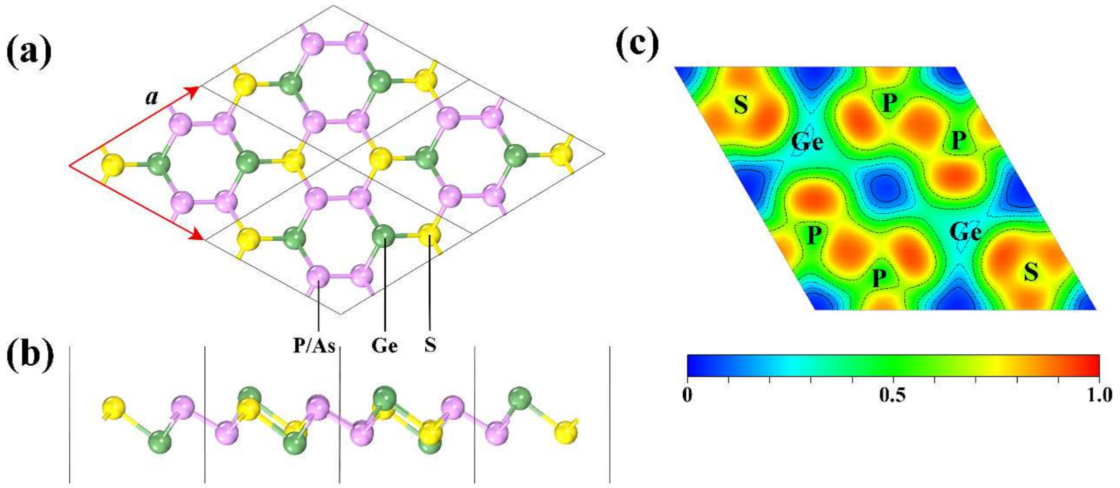

Fig. 1 (a) Top view and (b) side view of $Ge_2P(As)_4S_2$ monolayers in a 2×2×1 supercell. (c) Visualization of the electron localization function for monolayer $Ge_2P_4S_2$.

Table. 1 Calculated lattice constant a, buckling height h, cohesive energy E_c, amount of charge transfer T_B between different atoms, band gaps E_g (at both PBE and HSE06 levels) of $Ge_2P_4S_2$ and $Ge_2As_4S_2$ monolayers.

	a(Å)	h(Å)	E_c (eV/atom)	T_B(e)			E_g (eV)	
				Ge	S	P(As)	PBE	HSE06
$Ge_2P_4S_2$	6.77	1.91	3.40	-0.54	+0.57	-0.02	1.12	1.86
$Ge_2As_4S_2$	7.10	1.85	3.15	-0.43	+0.66	-0.12	1.21	1.89

In addition, the phonon spectra of $Ge_2P_4S_2$ and $Ge_2As_4S_2$ monolayers were calculated to examine their kinetic stability, as shown in **Figs. 2a and 2b**. No appreciable imaginary vibrational frequency modes are observed in the entire Brillouin zone for both $Ge_2P_4S_2$ and $Ge_2As_4S_2$ monolayers, proving that both two monolayers are kinetically stable. The thermal stability, however, can be tested by AIMD simulations at finite temperatures, where in our case the simulations were carried out at 500 K for 6 *ps*, with a time step of 1 *fs*. As shown in **Figs. 2c and 2d**, no obvious disruption of the geometries is found and the total energies fluctuate in a narrow range, suggesting robust thermodynamic stability of $Ge_2P_4S_2$ and $Ge_2As_4S_2$ monolayers up to 500 K. The mechanical stability of $Ge_2P_4S_2$/$Ge_2As_4S_2$ monolayers was further verified by calculating their linear elastic constants. As listed in **Table S1**, the elastic constants satisfy the corresponding mechanical stability conditions based on the Born criteria [53]: $C_{11}>0, C_{44}>0, C_{11}-C_{12}>0$. The kinetic, thermodynamic and mechanical stabilities pave the way for experimental realization of $Ge_2P_4S_2$ and $Ge_2As_4S_2$ monolayers.

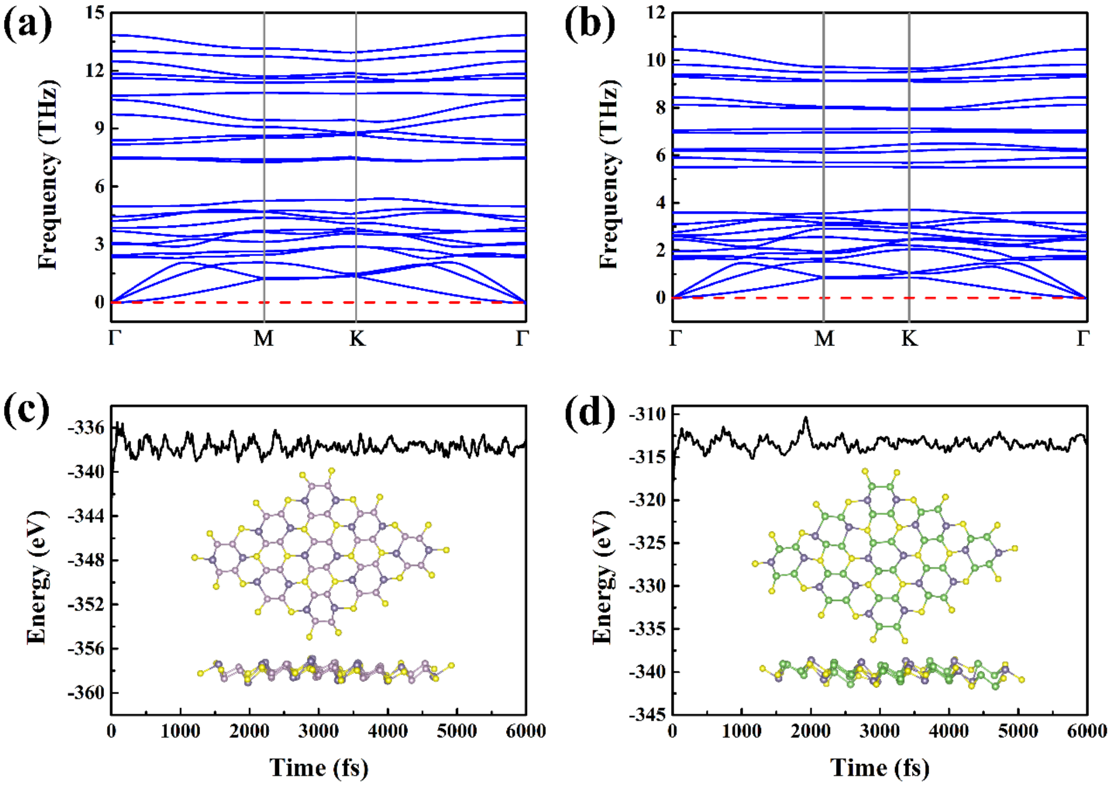

Fig. 2 Phonon band structures of (a) $Ge_2P_4S_2$, and (b) $Ge_2As_4S_2$ monolayers. The total energy fluctuations during AIMD simulations are shown for (c) $Ge_2P_4S_2$, and (d)

$Ge_2As_4S_2$ monolayers at 500K. The insets show snapshots of the structures after the 6 *ps* simulation time, in a 3 × 3 supercell.

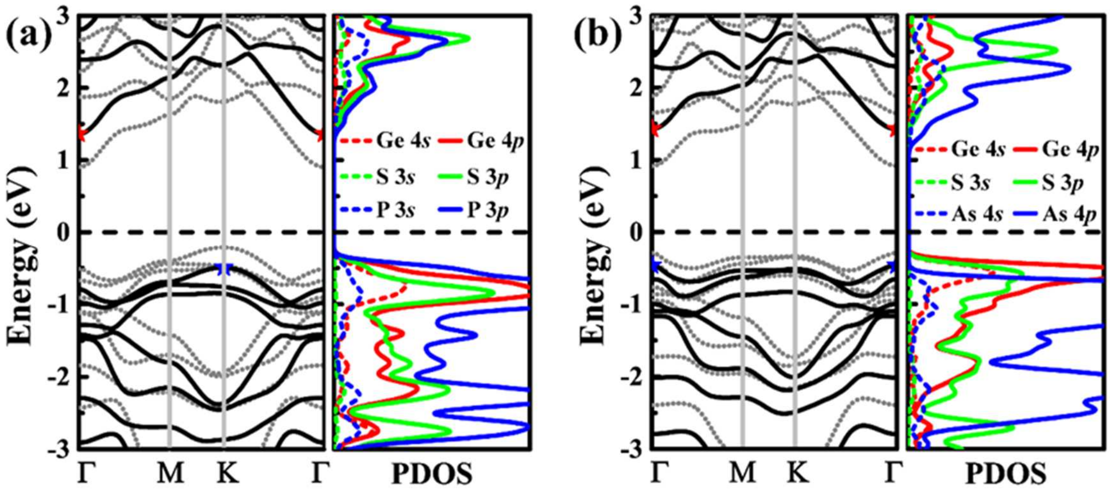

Fig. 3 Electronic band structure and projected density of states (PDOS) of (a) $Ge_2P_4S_2$ and (b) $Ge_2As_4S_2$ monolayers, calculated with the screened exchange HSE06 hybrid functional (solid line) and the PBE functional (dotted line). The pentagram points refer to VBM (blue) and CBM (red) locations, respectively.

3.2 Electronic structures and the strain effect

Figures 3a and 3b demonstrate the electronic band structures as well as the projected density of states (PDOS) of $Ge_2P_4S_2$/$Ge_2As_4S_2$ monolayers. Monolayer $Ge_2P_4S_2$ is a semiconductor with an indirect band gap of 1.85 eV according to our HSE06 calculation. The PBE-predicted gap value is 1.12 eV, which is also indirect, though with the well-known band gap underestimation. The VBM lies at the *K* point whereas the CBM is at the Γ point. Unlike the $Ge_2P_4S_2$ monolayer, however, the $Ge_2As_4S_2$ monolayer presents direct band gap feature with VBM/CBM both located at Γ. The band gap value is 1.89 eV based on the HSE06 calculation (1.21 eV for PBE). A PDOS analysis (the right column of **Fig. 3)** reveals that the conduction and valence bands involve contributions from all atoms in both materials. The VBM of $Ge_2P_4S_2$ ($Ge_2As_4S_2$) mainly consists of P 3*p* (As 4*p*), Ge 4*p*, S 3*p* and Ge 4*s* states, while the CBM of $Ge_2P_4S_2$ ($Ge_2As_4S_2$) mainly stems from S 3*p*, P 3*p* (As 4*p*) and Ge 4*p* states. In our electronic structure calculations, the spin-orbit coupling (SOC) effect was neglected, since we observed little impact on the band diagrams through turning on SOC, as confirmed by the band diagram comparison in **Fig. S1**.

Strain engineering is a feasible method to tune the band structure of 2D materials [54–58]. Hence, we further studied the evolution of band gap values upon the application of biaxial strain, using the PBE functional. Notwithstanding the issue of band gap underestimation, the consequence of strain on the band structure can be well described by PBE-calculations. **Figure 4** shows that the band gap increases gradually and then drops slowly upon varying the applied strain from -6% to 6%. Notably, the $Ge_2P_4S_2$ monolayer turns into a direct gap semiconductor by adding an extra 3% compressive strain (**Fig. 4a**), while the $Ge_2As_4S_2$ monolayer becomes indirect band gap with an applied tensile strain of 1% (**Fig. 4b**). Moreover, the calculated strain energy as a function of the biaxial strain is also given in these figures. The band structure evolution upon applying biaxial strain is reasonable (**Figs. 4c and 4d**), thus applying strain is an effective way to delicately tune the electronic properties of $Ge_2P(As)_4S_2$ monolayers.

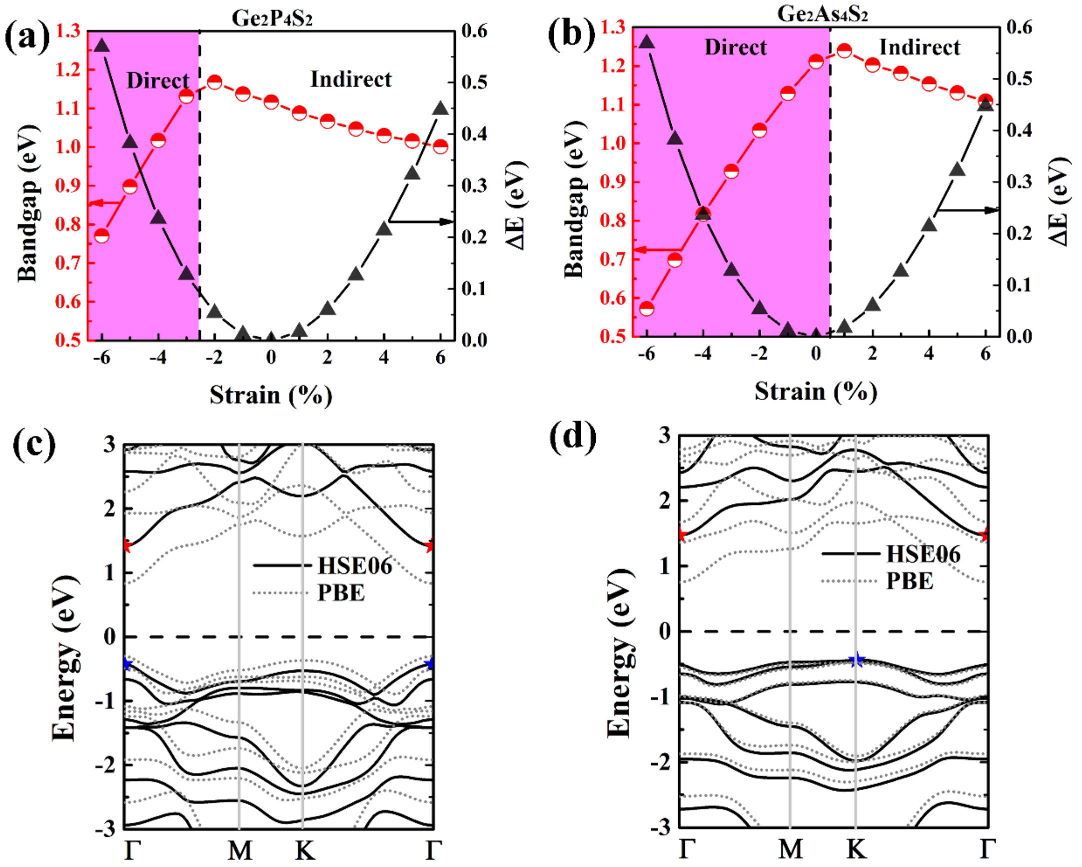

Fig. 4 Effect of strain effects on band gap and total energy (in energy variation ΔE) of (a) monolayer $Ge_2P_4S_2$, and (b) monolayer $Ge_2As_4S_2$. (c) The electronic band structure of $Ge_2P_4S_2$ with 3% compressive strain. (d) The electronic band structure of $Ge_2As_4S_2$ with 1% tensile strain using the screened exchange HSE06 hybrid functional (solid line) and the PBE functional (dotted line). The Fermi level is set to zero energy and the pentagram points indicate the VBM (blue) and CBM (red) locations, respectively.

3.3 Band alignments and optical properties

As the $Ge_2P_4S_2$ and $Ge_2As_4S_2$ monolayers possess suitable band gaps (>1.23 eV), it is worthwhile to explore their application potential as visible light photocatalysts. Yet, certain criteria of suitable band edges should be complied with, namely the position of CBM must be higher than the hydrogen reduction potential H^+/H_2 (-4.44 eV) while the VBM must be lower than the water oxidation potential of H_2O/O_2 (-5.67 eV). Our calculation results shown in **Fig. 5a** verify that the band edges of $Ge_2P_4S_2$ and $Ge_2As_4S_2$ monolayers perfectly cover the redox potentials of water, fulfilling the thermodynamic requirements for water splitting. Moreover, the $Ge_2P_4S_2$ monolayer with 3% compressive strain also has favorable band edge positions for water splitting, and the direct gap feature would make it more beneficial over the strain-free counterpart.

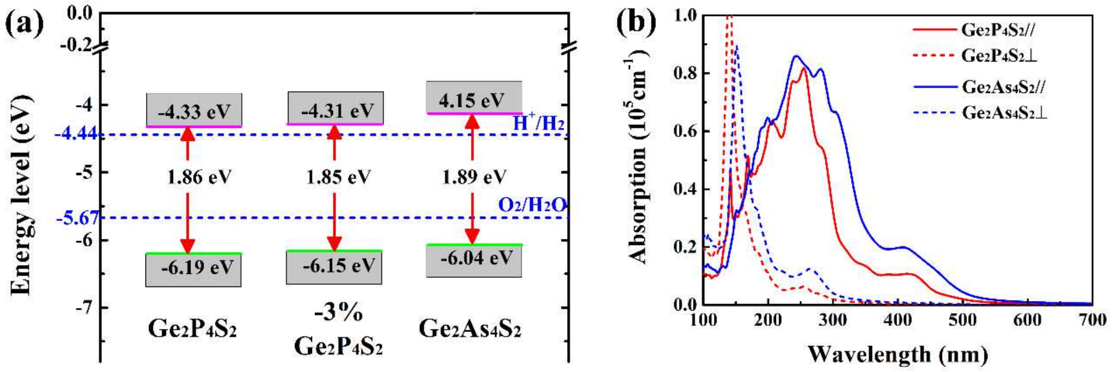

Fig. 5 (a) VBM and CBM locations of $Ge_2P_4S_2$ and $Ge_2As_4S_2$ monolayers with respect to the vacuum level (labeled as zero energy). The positions of the reduction potential of H^+ to H_2 and the oxidation potential of H_2O to O_2 are indicated by the blue dashed lines. (b) The calculated optical absorption coefficients of $Ge_2P_4S_2$/$Ge_2As_4S_2$ monolayers using the screened exchange HSE06 hybrid functional.

To efficiently harvest solar energy is another important requirement for photocatalysts. Hence, we further explored the optical properties of

$Ge_2P(As)_4S_2$ monolayers by calculating the in- and out-of-plane absorption spectra using the HSE06 functional. The transverse dielectric function $\varepsilon(\omega)=\varepsilon_1(\omega)+i\varepsilon_2(\omega)$ is used to describe the optical properties of materials, where ω is the photon frequency, $\varepsilon_1(\omega)$ and $\varepsilon_2(\omega)$ are the real and imaginary parts of the dielectric function, respectively. The absorption coefficient can be evaluated according to the expression [59] $\alpha(\omega)=\frac{\sqrt{2}\omega}{c}\left\{\left[\varepsilon_1^2(\omega)+\varepsilon_2^2(\omega)\right]^{\frac{1}{2}}-\varepsilon_1(\omega)\right\}^{\frac{1}{2}}$. As shown in **Fig. 5b**, the absorption coefficients of monolayer $Ge_2P(As)_4S_2$ reach the order of 10^5 cm^{-1}, which is comparable to that of the crystalline silicon for solar cells [60]. Out-of-plane absorption is larger than in-plane absorption in the invisible light region from 100 nm to 160 nm, while smaller than the latter in the wavelength region from 160 nm to ~600 nm. Overall, the $Ge_2P(As)_4S_2$ monolayers have considerable absorption in both ultraviolet and visible light regions.

3.4 Carrier mobility

Subsequently, we systematically calculated the carrier mobility (electrons and holes) based on the deformation potential (DP) theory proposed by Bardeen and Shockley [61]. The acoustic phonon-limited carrier mobility of homogeneous 2D materials can be evaluated by the following equation [62–64] $\mu_{2D}=\frac{e\hbar^3C_{2D}}{k_BTm^*m_d(E_1^i)^2}$, where $\hbar$ is the reduced Planck constant, k_B

is the Boltzmann constant, m^* is the effective mass in the direction of transport, m_d is the average effective mass determined by $m_d=(m_a^* m_b^*)^{1/2}$, and T is the temperature (T = 300 K). The elastic modulus C_{2D} of the longitudinal strain in the propagation direction is derived from $(E-E_0)/S_0=C_{2D}(\Delta l/l_0)^2/2$, where E is the total energy of the 2D structure, and S_0 is the lattice area of the equilibrium supercell. The deformation potential constant E_1^i is defined as $E_1^i=\Delta E_i/(\Delta l/l_0)$. Here ΔE_i is the energy change of the i^{th} band under proper cell compression and dilatation (calculated using a step of 0.5%), l_0 is the lattice constant in the transport direction and Δl is the deformation of l_0.

As summarized in **Table 2**, the effective masses of electrons and holes for $Ge_2P_4S_2$/$Ge_2As_4S_2$ monolayers along the a direction are 0.202/0.209 m_e and 1.669/0.123 m_e (m_e is the free electron mass), while those for the b direction are 0.395/0.836 m_e (for electrons) and 1.656/0.418 m_e (for holes), respectively. The elastic moduli are slightly anisotropic with the value of 54.14/48.46 N m^{-1} and 43.72/42.55 N m^{-1} for $Ge_2P_4S_2$ and $Ge_2As_4S_2$ monolayers along the a/b directions, respectively. The deformation potential constants E_l are small for $Ge_2P(As)_4S_2$, except for the hole of $Ge_2As_4S_2$ along the a direction (7.54 eV). Based on the values of m^*, C_{2D} and E_l, we estimated the carrier mobilities of $Ge_2P(As)_4S_2$ monolayers according to the Bardeen-Shockley formula. The electron mobilities of monolayer $Ge_2P_4S_2$ are as high as $1.22/1.56\times10^4$ cm^2 V^{-1} s^{-1} along *a*/*b* directions. In contrast to the high electron mobilities, the hole mobilities are relatively low with the value of $0.08/4.20\times10^3$ cm^2 V^{-1} s^{-1} along *a*/*b* directions, respectively. The low hole mobilities mainly stem from their large effective masses. For monolayer $Ge_2As_4S_2$, the electron and hole mobilities are 2.03/4.45 and $0.59/45.68\times10^3$ cm^2 V^{-1} s^{-1} along *a*/*b* directions, respectively. Note that for both materials the hole mobilities show great anisotropy, which implies that the homogeneous approximation is questionable, rendering the application of Bardeen-Shockley formula improper.

Therefore, we re-calculated the acoustic phonon-limited mobilities of $Ge_2P(As)_4S_2$ monolayers using a new formula proposed by Lang *et al.*, which considers the scattering from the other direction in 2D semiconductors [65]. The carrier mobility along the *a*-axis of anisotropic 2D materials can be calculated using the following equation [65]

$$\mu_a = \frac{e\hbar^3\left(\frac{5C_a^{2D}+3C_b^{2D}}{8}\right)}{k_\mathrm{B}T(m_a)^{\frac{3}{2}}(m_b)^{\frac{1}{2}}\left(\frac{9E_{1a}^2+7E_{1a}E_{1b}+4E_{1b}^2}{20}\right)^2}.$$

Through this formula, one can take into the account the anisotropic elastic constants or deformation potential constants, which in general tends to reduce the strong anisotropy stemming from the Bardeen-Shockley formula [66,67]. For monolayer $Ge_2P_4S_2$, Lang *et al.*'s formula yields electron mobilities of 1.61×10^4 cm^2 V^{-1} s^{-1} and 1.02×10^4 cm^2 V^{-1} s^{-1} along the *a* and *b* directions, respectively. For holes, the large anisotropy is greatly diminished, yielding 150 cm^2 V^{-1} s^{-1} and 280 cm^2 V^{-1} s^{-1} along the *a* and *b* directions, respectively. Compared with monolayer $Ge_2P_4S_2$, however, the hole mobilities of monolayer $Ge_2As_4S_2$ are homogenized to 1.24×10^3 cm^2 V^{-1} s^{-1} and 760 cm^2 V^{-1} s^{-1} along the *a* and *b* directions, respectively. And for electrons, the mobilities are 3.42×10^3 cm^2 V^{-1} s^{-1} and 1.37×10^3 cm^2 V^{-1} s^{-1} cm^2 V^{-1} s^{-1} along the *a* and *b* directions, where the *a*-direction now becomes the fast-transport direction. After fixing the treatment of carrier mobility anisotropy, the generally high carrier mobilities are still confirmed in $Ge_2P(As)_4S_2$ monolayers.

Table 2. Calculated effective mass m^* (unit: m_e), deformation potential constant $\lvert E_1^i \rvert$ (unit: eV), elastic modulus C_{2D} (unit: N m^{-1}), carrier mobility μ_{2D} (unit: 10^3 cm^2 $V^{-1}s^{-1}$) for monolayer $Ge_2P_4S_2$/$Ge_2As_4S_2$ along the *a* and *b* directions. For mobility, two distinct values are listed in the format of α/β, where α was obtained directly from the Bardeen–Shockley formula while β (underlined) was obtained using the new theory proposed by Lang *et al.* [65].

Materials	Carrier type	m_a^*	m_b^*	$\lvert E_{1a} \rvert$	$\lvert E_{1b} \rvert$	C_a^{2D}	C_b^{2D}	μ_a^{2D}	μ_b^{2D}
$Ge_2P_4S_2$	Electron	0.202	0.395	1.29	0.77	54.14	48.46	12.24/**16.06**	15.59/**10.23**
	Hole	1.669	1.656	2.35	0.30	54.14	48.46	0.08/**0.15**	4.20/**0.28**
$Ge_2As_4S_2$	Electron	0.209	0.836	2.29	0.76	43.72	42.55	2.03/**3.42**	4.45/**1.37**
	Hole	0.123	0.418	7.53	0.46	43.72	42.55	0.59/**1.24**	45.68/**0.76**

3.5 Water adsorption and decomposition on the surface of 2D

$Ge_2As_4S_2$

Last but not least, we have investigated the stability of $Ge_2P(As)_4S_2$ monolayers in liquid water, which is essential for their practical implementation as photocatalysts. To this end, AIMD simulations were performed at room temperature (300 K) with a time scale of 6 *ps*. Owing to the structural similarity, monolayer $Ge_2As_4S_2$ was chosen to be the representative model system for both materials. Our results in **Fig. S2** demonstrate that monolayer $Ge_2As_4S_2$ is still thermodynamically stable in liquid water at room temperature. The redox reactions of water on monolayer $Ge_2As_4S_2$ were also investigated to further reveal the mechanism of photocatalytic hydrogen evolution. The adsorption energy of a species or functional group X on a 2D surface can be defined as

$$E_{\mathrm{ad}} = E(\text{2D-X}) - E(\text{2D}) - \mu_{\mathrm{x}}$$

where $E(\text{2D-X})$ and $E(\text{2D})$ are the total energies of the 2D material with and without the adsorbed X, respectively; μ_X is the chemical potential of X. We specify the chemical potential of water as the total energy of an isolated H_2O molecule. Yet, the chemical potentials of –H and –OH suffer from uncertainties. Here, two schemes are proposed: (1) their chemical potentials equal the total energies of isolated neutral H and OH function groups; (2) μ_{H} is chosen as a half of the H_2 molecule energy, while μ_{OH} satisfies $\mu_{\mathrm{OH}} + \mu_{\mathrm{H}} = \mu_{\mathrm{water}}$. The first scheme is consistent with several previously published works [20,68–71], but the second scheme considers that the source of surface –H and –OH is mainly water molecules. According to Scheme 1, the adsorption energies of H, OH and H_2O on monolayer $Ge_2As_4S_2$ are -1.71 eV, -2.58 eV and -0.30 eV, respectively, favoring their surface adsorption. Using Scheme 2, we find the corresponding adsorption energies of H and OH become 0.56 eV and 0.52 eV, while the adsorption energy of H_2O is the same (-0.30 eV) by definition. It should be noted that the reaction energy of subsequent water decomposition on monolayer $Ge_2As_4S_2$ is from -0.30 eV to 0.71 eV, indicating an endothermic reaction, which is similar to the water decomposition reaction on anatase TiO_2 surface [72]. In addition, the remotely separated hydrogen adatoms prefer to migrate close to each other, forming hydrogen molecules, when the photo-generated hydrogen atoms are adsorbed on monolayer $Ge_2As_4S_2$ (**Fig. 6b**). It is beneficial that the endothermic reaction energy required for removing one H_2 molecule from monolayer $Ge_2As_4S_2$ is only 0.05 eV, facilitating the release of produced H_2 from the surface, which is similar to the case of Zr_2CO_2 [20] and GeS [69]. These encouraging results list monolayer $Ge_2As_4S_2$ as an excellent candidate for photocatalytic water splitting.

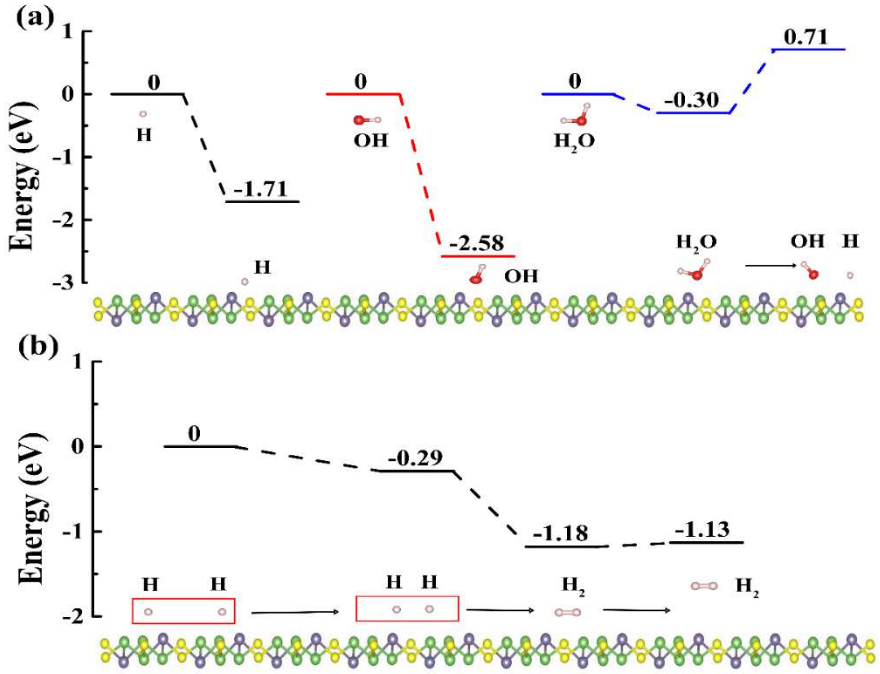

Fig. 6 (a) Adsorption configurations of H, OH, and H_2O, and decomposition mechanism of H_2O on monolayer $Ge_2As_4S_2$. (b) Interaction between two hydrogen adatoms, showing the formation and releasing of hydrogen molecules on/from monolayer $Ge_2As_4S_2$.

4. Conclusion

To summarize, the structural, electronic and optical properties of $Ge_2P_4S_2$/$Ge_2As_4S_2$ monolayers were investigated systematically through density functional theory calculations. The cohesive energy, phonon dispersions as well as AIMD simulation results demonstrate the high stability of $Ge_2P_4S_2$ and $Ge_2As_4S_2$ monolayers. Monolayer $Ge_2As_4S_2$ has a direct Γ-Γ band gap of 1.89 eV, while monolayer $Ge_2P_4S_2$ is an indirect band gap semiconductor with 1.85 eV gap value, which can become direct band gap by applying 3% compressive strain. Attractively, the band edge positions of $Ge_2P(As)_4S_2$ monolayers perfectly meet the requirement of the reduction and oxidation levels for water splitting. Moreover, the $Ge_2P_4S_2$ and $Ge_2As_4S_2$ monolayers show great anisotropy, and the highest acoustic phonon-limited electron mobilities are 1.606×10^4 cm^2 V^{-1} s^{-1} and 3.42×10^3 cm^2 V^{-1} s^{-1}, respectively. Their high carrier mobilities and moderate optical absorption in the visible-light wavelengths add to their application potential in photocatalytic water splitting.

Acknowledgement

This work was supported by the National Natural Science Foundation of China under Grant No. 11704134, and the Hubei "Chu-Tian Young Scholar" program. K.-H. Xue received support the China Scholarship Council (No. 201806165012).

Appendix A. Supplementary data

Supplementary data to this article can be found online.

Reference

[1] Maeda K, Domen K. New Non-Oxide Photocatalysts Designed for Overall Water Splitting under Visible Light. The Journal of Physical Chemistry C 2007;111:7851–61. doi:10.1021/jp070911w.

[2] Youngblood WJ, Lee S-HA, Maeda K, Mallouk TE. Visible Light Water Splitting Using

Dye-Sensitized Oxide Semiconductors. Accounts of Chemical Research 2009;42:1966–73. doi:10.1021/ar9002398.

[3] Fajrina N, Tahir M. A critical review in strategies to improve photocatalytic water splitting towards hydrogen production. International Journal of Hydrogen Energy 2019;44:540–77. doi:10.1016/j.ijhydene.2018.10.200.

[4] Lin H-Y, Chang Y-S. Photocatalytic water splitting on Au/HTiNbO5 nanosheets. International Journal of Hydrogen Energy 2014;39:3118–26. doi:10.1016/j.ijhydene.2013.12.094.

[5] Navakoteswara Rao V, Lakshmana Reddy N, Mamatha Kumari M, Ravi P, Sathish M, Kuruvilla KM, et al. Photocatalytic recovery of H2 from H2S containing wastewater: Surface and interface control of photo-excitons in Cu2S@TiO2 core-shell nanostructures. Applied Catalysis B: Environmental 2019;254:174–85. doi:10.1016/j.apcatb.2019.04.090.

[6] Pulipaka S, Koushik AKS, Boni N, Deepa M, Meduri P. Tin disulfide based ternary composites for visible light driven photoelectrochemical water splitting. International Journal of Hydrogen Energy 2019;44:11584–92. doi:10.1016/j.ijhydene.2019.03.135.

[7] Ehrmaier J, Janicki MJ, Sobolewski AL, Domcke W. Mechanism of photocatalytic water splitting with triazine-based carbon nitrides: insights from *ab initio* calculations for the triazine–water complex. Physical Chemistry Chemical Physics 2018;20:14420–30. doi:10.1039/C8CP01998C.

[8] Ehrmaier J, Karsili TNV, Sobolewski AL, Domcke W. Mechanism of Photocatalytic Water Splitting with Graphitic Carbon Nitride: Photochemistry of the Heptazine–Water Complex. The Journal of Physical Chemistry A 2017;121:4754–64. doi:10.1021/acs.jpca.7b04594.

[9] Fujishima A, Honda K. Electrochemical Photolysis of Water at a Semiconductor Electrode. Nature 1972;238:37–8. doi:10.1038/238037a0.

[10] Tabata M, Maeda K, Higashi M, Lu D, Takata T, Abe R, et al. Modified Ta $_3$ N $_5$ Powder as a Photocatalyst for O $_2$ Evolution in a Two-Step Water Splitting System with an Iodate/Iodide Shuttle Redox Mediator under Visible Light. Langmuir 2010;26:9161–5. doi:10.1021/la100722w.

[11] Ding Z, Hu H, Xu J, Lin P, Cui C, Qian D, et al. Hierarchical spheres assembled from large ultrathin anatase TiO 2 nanosheets for photocatalytic hydrogen evolution from water

splitting. International Journal of Hydrogen Energy 2018;43:13190–9. doi:10.1016/j.ijhydene.2018.05.071.

[12] Lin Y, Yang S, Liu Y, Zhang S, Wang H, Yu H, et al. In-situ photo-deposition CuO1− cluster on TiO2 for enhanced photocatalytic H2-production activity. International Journal of Hydrogen Energy 2017;42:19942 – 50. doi:10.1016/j.ijhydene.2017.06.094.

[13] Liu Y, Yang S, Zhang S, Wang H, Yu H, Cao Y, et al. Design of cocatalyst loading position for photocatalytic water splitting into hydrogen in electrolyte solutions. International Journal of Hydrogen Energy 2018;43:5551–60. doi:10.1016/j.ijhydene.2018.01.115.

[14] Wang X, Zhang S, Xie Y, Wang H, Yu H, Shen Y, et al. Branched hydrogenated TiO 2 nanorod arrays for improving photocatalytic hydrogen evolution performance under simulated solar light. International Journal of Hydrogen Energy 2016;41:20192–7. doi:10.1016/j.ijhydene.2016.09.029.

[15] Yang S, Wang H, Yu H, Zhang S, Fang Y, Zhang S, et al. A facile fabrication of hierarchical Ag nanoparticles-decorated N-TiO 2 with enhanced photocatalytic hydrogen production under solar light. International Journal of Hydrogen Energy 2016;41:3446–55. doi:10.1016/j.ijhydene.2015.12.190.

[16] Kudo A, Miseki Y. Heterogeneous photocatalyst materials for water splitting. Chem Soc Rev 2009;38:253–78. doi:10.1039/B800489G.

[17] Phoon BL, Lai CW, Juan JC, Show P-L, Pan G-T. Recent developments of strontium titanate for photocatalytic water splitting application. International Journal of Hydrogen Energy 2019:S0360319919303246. doi:10.1016/j.ijhydene.2019.01.166.

[18] Ni M, Leung MKH, Leung DYC, Sumathy K. A review and recent developments in photocatalytic water-splitting using TiO2 for hydrogen production. Renewable and Sustainable Energy Reviews 2007;11:401–25. doi:10.1016/j.rser.2005.01.009.

[19] Cook TR, Dogutan DK, Reece SY, Surendranath Y, Teets TS, Nocera DG. Solar Energy Supply and Storage for the Legacy and Nonlegacy Worlds. Chemical Reviews 2010;110:6474–502. doi:10.1021/cr100246c.

[20] Guo Z, Zhou J, Zhu L, Sun Z. MXene: a promising photocatalyst for water splitting. Journal of Materials Chemistry A 2016;4:11446–52. doi:10.1039/C6TA04414J.

[21] Ran J, Zhang J, Yu J, Jaroniec M, Qiao SZ. Earth-abundant cocatalysts for

semiconductor-based photocatalytic water splitting. Chem Soc Rev 2014;43:7787–812. doi:10.1039/C3CS60425J.

[22] Singh AK, Mathew K, Zhuang HL, Hennig RG. Computational Screening of 2D Materials for Photocatalysis. The Journal of Physical Chemistry Letters 2015;6:1087–98. doi:10.1021/jz502646d.

[23] Chen X, Liu L, Yu PY, Mao SS. Increasing Solar Absorption for Photocatalysis with Black Hydrogenated Titanium Dioxide Nanocrystals. Science 2011;331:746–50. doi:10.1126/science.1200448.

[24] Li Y, Li Y-L, Sa B, Ahuja R. Review of two-dimensional materials for photocatalytic water splitting from a theoretical perspective. Catalysis Science & Technology 2017;7:545–59. doi:10.1039/C6CY02178F.

[25] Qiao M, Liu J, Wang Y, Li Y, Chen Z. PdSeO $_3$ Monolayer: Promising Inorganic 2D Photocatalyst for Direct Overall Water Splitting Without Using Sacrificial Reagents and Cocatalysts. Journal of the American Chemical Society 2018;140:12256–62. doi:10.1021/jacs.8b07855.

[26] Su T, Shao Q, Qin Z, Guo Z, Wu Z. Role of Interfaces in Two-Dimensional Photocatalyst for Water Splitting. ACS Catalysis 2018;8:2253–76. doi:10.1021/acscatal.7b03437.

[27] Sun Y, Sun Z, Gao S, Cheng H, Liu Q, Piao J, et al. Fabrication of flexible and freestanding zinc chalcogenide single layers. Nature Communications 2012;3. doi:10.1038/ncomms2066.

[28] Liao J, Sa B, Zhou J, Ahuja R, Sun Z. Design of High-Efficiency Visible-Light Photocatalysts for Water Splitting: MoS $_2$ /AlN(GaN) Heterostructures. The Journal of Physical Chemistry C 2014;118:17594–9. doi:10.1021/jp5038014.

[29] Wang X, Maeda K, Thomas A, Takanabe K, Xin G, Carlsson JM, et al. A metal-free polymeric photocatalyst for hydrogen production from water under visible light. Nature Materials 2009;8:76–80. doi:10.1038/nmat2317.

[30] Mishra A, Mehta A, Basu S, Shetti NP, Reddy KR, Aminabhavi TM. Graphitic carbon nitride (g–C3N4)–based metal-free photocatalysts for water splitting: A review. Carbon 2019;149:693–721. doi:10.1016/j.carbon.2019.04.104.

[31] Reddy KR, Reddy CHV, Nadagouda MN, Shetti NP, Jaesool S, Aminabhavi TM. Polymeric graphitic carbon nitride (g-C3N4)-based semiconducting nanostructured materials:

Synthesis methods, properties and photocatalytic applications. Journal of Environmental Management 2019;238:25–40. doi:10.1016/j.jenvman.2019.02.075.

[32] Zhuang HL, Hennig RG. Single-Layer Group-III Monochalcogenide Photocatalysts for Water Splitting. Chemistry of Materials 2013;25:3232–8. doi:10.1021/cm401661x.

[33] Jing Y, Ma Y, Li Y, Heine T. GeP $_3$: A Small Indirect Band Gap 2D Crystal with High Carrier Mobility and Strong Interlayer Quantum Confinement. Nano Letters 2017;17:1833–8. doi:10.1021/acs.nanolett.6b05143.

[34] Yao S, Zhang X, Zhang Z, Chen A, Zhou Z. 2D Triphosphides: SbP3 and GaP3 monolayer as promising photocatalysts for water splitting. International Journal of Hydrogen Energy 2019;44:5948–54. doi:10.1016/j.ijhydene.2019.01.106.

[35] Miao N, Xu B, Bristowe NC, Zhou J, Sun Z. Tunable Magnetism and Extraordinary Sunlight Absorbance in Indium Triphosphide Monolayer. J Am Chem Soc 2017;139:11125–31. doi:10.1021/jacs.7b05133.

[36] Sun S, Meng F, Wang H, Wang H, Ni Y. Novel two-dimensional semiconductor SnP $_3$: high stability, tunable bandgaps and high carrier mobility explored using first-principles calculations. Journal of Materials Chemistry A 2018;6:11890–7. doi:10.1039/C8TA02494D.

[37] Yuan J-H, Cresti A, Xue K-H, Song Y-Q, Su H-L, Li L-H, et al. TlP $_5$: an unexplored direct band gap 2D semiconductor with ultra-high carrier mobility. J Mater Chem C 2019;7:639–44. doi:10.1039/C8TC05164J.

[38] Ghosh B, Puri S, Agarwal A, Bhowmick S. SnP $_3$: A Previously Unexplored Two-Dimensional Material. The Journal of Physical Chemistry C 2018;122:18185–91. doi:10.1021/acs.jpcc.8b06668.

[39] Andriotis AN, Richter E, Menon M. Prediction of a new graphenelike Si 2 BN solid. Physical Review B 2016;93. doi:10.1103/PhysRevB.93.081413.

[40] Xie Q, Yuan J, Yu N, Wang L, Wang J. Prediction of new group IV-V-VI monolayer semiconductors based on first principle calculation. Computational Materials Science 2017;135:160–4. doi:10.1016/j.commatsci.2017.04.005.

[41] Ding Y, Wang Y. Tunable electronic and magnetic properties of graphene-like XYBe $_3$ (XY = BN, AlN, SiC, GeC) nanosheets with carrier doping: a first-principles study. Physical Chemistry Chemical Physics 2018;20:6830–7. doi:10.1039/C7CP06862J.

[42] Kresse G, Furthmüller J. Efficient iterative schemes for ab initio total-energy calculations using a plane-wave basis set. Phys Rev B 1996;54:11169–86. doi:10.1103/PhysRevB.54.11169.

[43] Kresse G, Joubert D. From ultrasoft pseudopotentials to the projector augmented-wave method. Phys Rev B 1999;59:1758–75. doi:10.1103/PhysRevB.59.1758.

[44] Perdew JP, Burke K, Ernzerhof M. Generalized Gradient Approximation Made Simple. Phys Rev Lett 1996;77:3865–8. doi:10.1103/PhysRevLett.77.3865.

[45] Heyd J, Scuseria GE, Ernzerhof M. Hybrid functionals based on a screened Coulomb potential. The Journal of Chemical Physics 2003;118:8207–15. doi:10.1063/1.1564060.

[46] Chaput L, Togo A, Tanaka I, Hug G. Phonon-phonon interactions in transition metals. Physical Review B 2011;84. doi:10.1103/PhysRevB.84.094302.

[47] Togo A, Oba F, Tanaka I. First-principles calculations of the ferroelastic transition between rutile-type and ${\text{CaCl}}_{2}$-type ${\text{SiO}}_{2}$ at high pressures. Phys Rev B 2008;78:134106. doi:10.1103/PhysRevB.78.134106.

[48] Martyna GJ, Klein ML, Tuckerman M. Nosé–Hoover chains: The canonical ensemble via continuous dynamics. The Journal of Chemical Physics 1992;97:2635–43. doi:10.1063/1.463940.

[49] Silvi B, Savin A. Classification of chemical bonds based on topological analysis of electron localization functions. Nature 1994;371:683–6. doi:10.1038/371683a0.

[50] Henkelman G, Arnaldsson A, Jónsson H. A fast and robust algorithm for Bader decomposition of charge density. Computational Materials Science 2006;36:354–60. doi:10.1016/j.commatsci.2005.04.010.

[51] Chen Y, Sun Q, Jena P. SiTe monolayers: Si-based analogues of phosphorene. Journal of Materials Chemistry C 2016;4:6353–61. doi:10.1039/C6TC01138A.

[52] Guan J, Zhu Z, Tománek D. Phase Coexistence and Metal-Insulator Transition in Few-Layer Phosphorene: A Computational Study. Physical Review Letters 2014;113. doi:10.1103/PhysRevLett.113.046804.

[53] Beckstein O, Klepeis JE, Hart GLW, Pankratov O. First-principles elastic constants and electronic structure of α − Pt 2 Si and PtSi. Physical Review B 2001;63. doi:10.1103/PhysRevB.63.134112.

[54] Hu T, Zhou J, Dong J. Strain induced new phase and indirect–direct band gap transition of monolayer InSe. Physical Chemistry Chemical Physics 2017;19:21722–8. doi:10.1039/C7CP03558F.

[55] Kamal C, Ezawa M. Arsenene: Two-dimensional buckled and puckered honeycomb arsenic systems. Physical Review B 2015;91. doi:10.1103/PhysRevB.91.085423.

[56] Lü T-Y, Liao X-X, Wang H-Q, Zheng J-C. Tuning the indirect–direct band gap transition of SiC, GeC and SnC monolayer in a graphene-like honeycomb structure by strain engineering: a quasiparticle GW study. Journal of Materials Chemistry 2012;22:10062. doi:10.1039/c2jm30915g.

[57] Yuan J, Yu N, Xue K, Miao X. Ideal strength and elastic instability in single-layer 8- Pmmn borophene. RSC Advances 2017;7:8654–60. doi:10.1039/C6RA28454J.

[58] Zhang S, Yan Z, Li Y, Chen Z, Zeng H. Atomically Thin Arsenene and Antimonene: Semimetal-Semiconductor and Indirect-Direct Band-Gap Transitions. Angewandte Chemie International Edition 2015;54:3112–5. doi:10.1002/anie.201411246.

[59] Yuan J-H, Gao B, Wang W, Wang J-F. First-Principles Calculations of the Electronic Structure and Optical Properties of Y-Cu Co-Doped ZnO. Acta Physico-Chimica Sinca 2015;31:1302–8. doi:10.3866/PKU.WHXB201505081.

[60] Green MA, Keevers MJ. Optical properties of intrinsic silicon at 300 K. Progress in Photovoltaics: Research and Applications 1995;3:189–92. doi:10.1002/pip.4670030303.

[61] Bardeen J, Shockley W. Deformation Potentials and Mobilities in Non-Polar Crystals. Physical Review 1950;80:72–80. doi:10.1103/PhysRev.80.72.

[62] Qiao J, Kong X, Hu Z-X, Yang F, Ji W. High-mobility transport anisotropy and linear dichroism in few-layer black phosphorus. Nature Communications 2014;5. doi:10.1038/ncomms5475.

[63] Xie J, Zhang ZY, Yang DZ, Xue DS, Si MS. Theoretical Prediction of Carrier Mobility in Few-Layer BC_2N. The Journal of Physical Chemistry Letters 2014;5:4073–7. doi:10.1021/jz502006z.

[64] Cai Y, Zhang G, Zhang Y-W. Polarity-Reversed Robust Carrier Mobility in Monolayer MoS_2 Nanoribbons. Journal of the American Chemical Society 2014;136:6269–75. doi:10.1021/ja4109787.

[65] Lang H, Zhang S, Liu Z. Mobility anisotropy of two-dimensional semiconductors. Physical Review B 2016;94. doi:10.1103/PhysRevB.94.235306.

[66] Zhou M, Chen X, Li M, Du A. Widely tunable and anisotropic charge carrier mobility in monolayer tin(II) selenide using biaxial strain: a first-principles study. Journal of Materials Chemistry C 2017;5:1247–54. doi:10.1039/C6TC04692D.

[67] Song Y-Q, Yuan J-H, Li L-H, Xu M, Wang J-F, Xue K-H, et al. KTlO: a metal shrouded 2D semiconductor with high carrier mobility and tunable magnetism. Nanoscale 2019;11:1131–9. doi:10.1039/C8NR08046A.

[68] Peng Q, Xiong R, Sa B, Zhou J, Wen C, Wu B, et al. Computational mining of photocatalysts for water splitting hydrogen production: two-dimensional InSe-family monolayers. Catal Sci Technol 2017;7:2744–52. doi:10.1039/C7CY00090A.

[69] Lv X, Wei W, Sun Q, Li F, Huang B, Dai Y. Two-dimensional germanium monochalcogenides for photocatalytic water splitting with high carrier mobility. Applied Catalysis B: Environmental 2017;217:275–84. doi:10.1016/j.apcatb.2017.05.087.

[70] Meng R, Sun X, Yang D, Bao J, Chen X. Two dimensional XAs (X = Si, Ge, Sn) monolayers as promising photocatalysts for water splitting hydrogen production with high carrier mobility. Applied Materials Today 2018;13:276–84. doi:10.1016/j.apmt.2018.09.013.

[71] Chowdhury C, Karmakar S, Datta A. Monolayer Group IV–VI Monochalcogenides: Low-Dimensional Materials for Photocatalytic Water Splitting. The Journal of Physical Chemistry C 2017;121:7615–24. doi:10.1021/acs.jpcc.6b12080.

[72] Zhao Z, Li Z, Zou Z. A Theoretical Study of Water Adsorption and Decomposition on the Low-Index Stoichiometric Anatase TiO $_2$ Surfaces. The Journal of Physical Chemistry C 2012;116:7430–41. doi:10.1021/jp212407s.

Support Information for

Promising photocatalysts with high carrier mobility for water splitting in monolayer $Ge_2P_4S_2$ and $Ge_2As_4S_2$

Yun-Lai Zhu,[a+] Jun-Hui Yuan,[a+] Ya-Qian Song,[a] Kan-Hao Xue,[a,b*] Sheng Wang,[a] Chen Lian,[a] Zhao-Nan Li,[a] Ming Xu,[a] Xiao-Min Cheng,[a*] Xiang-Shui Miao[a]

[a]Wuhan National Research Center for Optoelectronics, School of Optical and Electronic Information, Huazhong University of Science and Technology, Wuhan 430074, China

[b] Univ. Grenoble Alpes, Univ. Savoie Mont Blanc, CNRS, Grenoble INP, IMEP-LAHC, 38000 Grenoble, France

[+]The authors Y.-L. Zhu and J.-H. Yuan contributed equally to this work.

Corresponding Authors

*E-mail: xmcheng@hust.edu.cn (X.-M. Cheng) xkh@hust.edu.cn (K.-H. Xue)

The 2D elastic constants matrix components C_{11}, C_{12}, C_{22} and C_{44} of $Ge_2P_4S_2$ and $Ge_2As_4S_2$ monolayers are calculated, as listed in **Table S1**. For 2D materials, the corresponding mechanical stability conditions based on the Born criteria[1] are $C_{11} > 0, C_{44} > 0, C_{11} - C_{12} > 0$.[2] Obviously, the elastic constants stratify above mentioned conditions, suggesting that the $Ge_2P_4S_2$ and $Ge_2As_4S_2$ monolayers are mechanically stable. Furthermore, the Young's modulus E_x (E_y) is defined as $E_x = C_{11} - \frac{C_{12}^2}{C_{22}}, E_y = C_{22} - \frac{C_{12}^2}{C_{11}}$.[3] It can be observed that E_x and E_y are very close both for the $Ge_2P_4S_2$ and $Ge_2As_4S_2$ monolayers, indicating the weak structural anisotropy. The

Young's modulus of $Ge_2P_4S_2$ monolayer along the *x* and *y* direction are 46.89 and 49.84 N m^{-1}, while that is 42.12 (*x* direction) and 43.45 N m^{-1}(*y* direction) for $Ge_2As_4S_2$ monolayer, respectively. Compared to other 2D materials, the Young's modulus of $Ge_2P_4S_2$ and $Ge_2As_4S_2$ monolayers are smaller than that of graphene (344.2 N m^{-1}) [4] and MoS_2 (130N m^{-1})[5] monolayers, indicating that the $Ge_2P_4S_2$ and $Ge_2As_4S_2$ monolayers are rather flexible material.

Table S1 Effective independent elastic constants (C_{ij}, in N m^{-1}), and Young's moduli (E_x, E_y, in N m^{-1}) of $Ge_2P_4S_2$ and $Ge_2As_4S_2$ monolayers.

	C_{11}	C_{12}	C_{22}	C_{44}	E_x	E_y
$Ge_2P_4S_2$	47.59	5.94	50.48	21.48	46.89	49.84
$Ge_2As_4S_2$	43.37	7.48	44.74	18.20	42.12	43.45

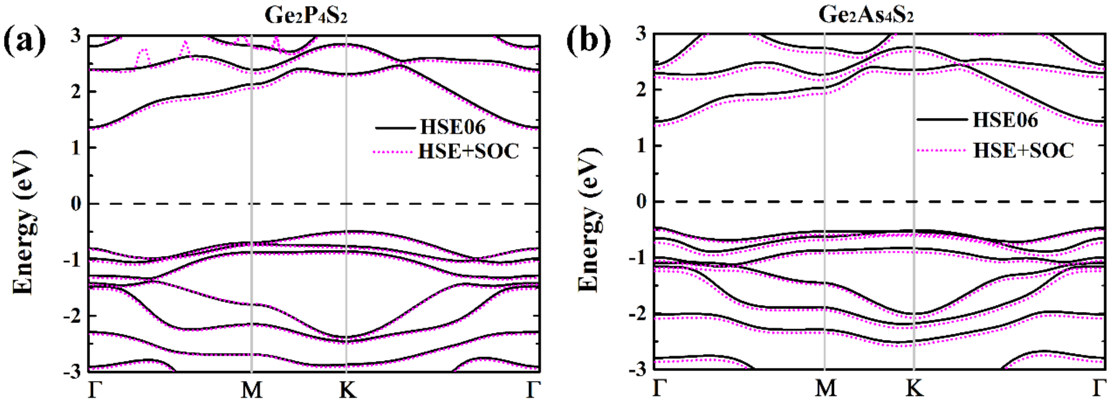

Fig. S1 The band structures of monolayer (a) $Ge_2P_4S_2$; and (b) $Ge_2As_4S_2$ with/without spin-orbit coupling (SOC) effects using HSE06 functional.

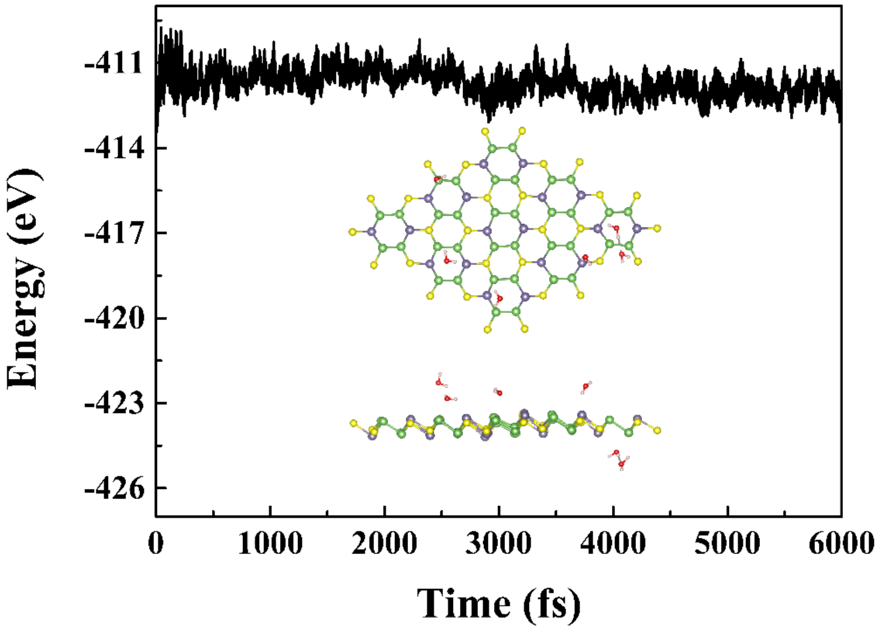

Fig. S2 The vibration of the total energies for $Ge_2As_4S_2$ monolayers during *ab initio* molecular dynamics (AIMD) simulations in the water environment at 300K. The insets show snapshots of the structures after the 6 *ps* simulation time with 3 × 3 supercell with six water molecule.

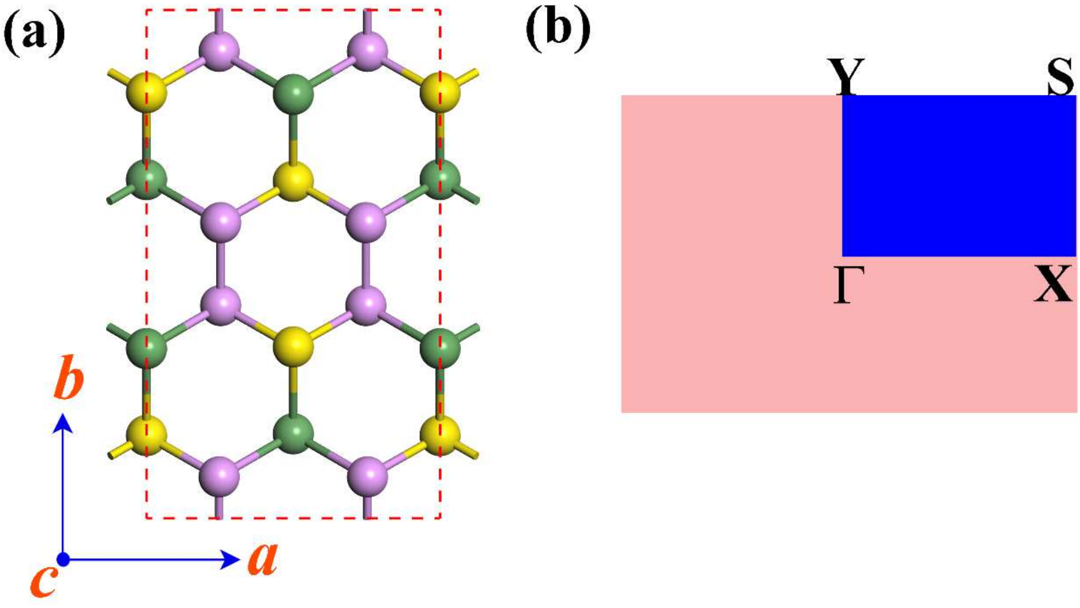

Fig. S3 (a) Crystal structure and (b) the corresponding first Brillouin zone with high symmetry points of $Ge_2P(As)_4S_2$ monolayers in an orthogonal supercell.

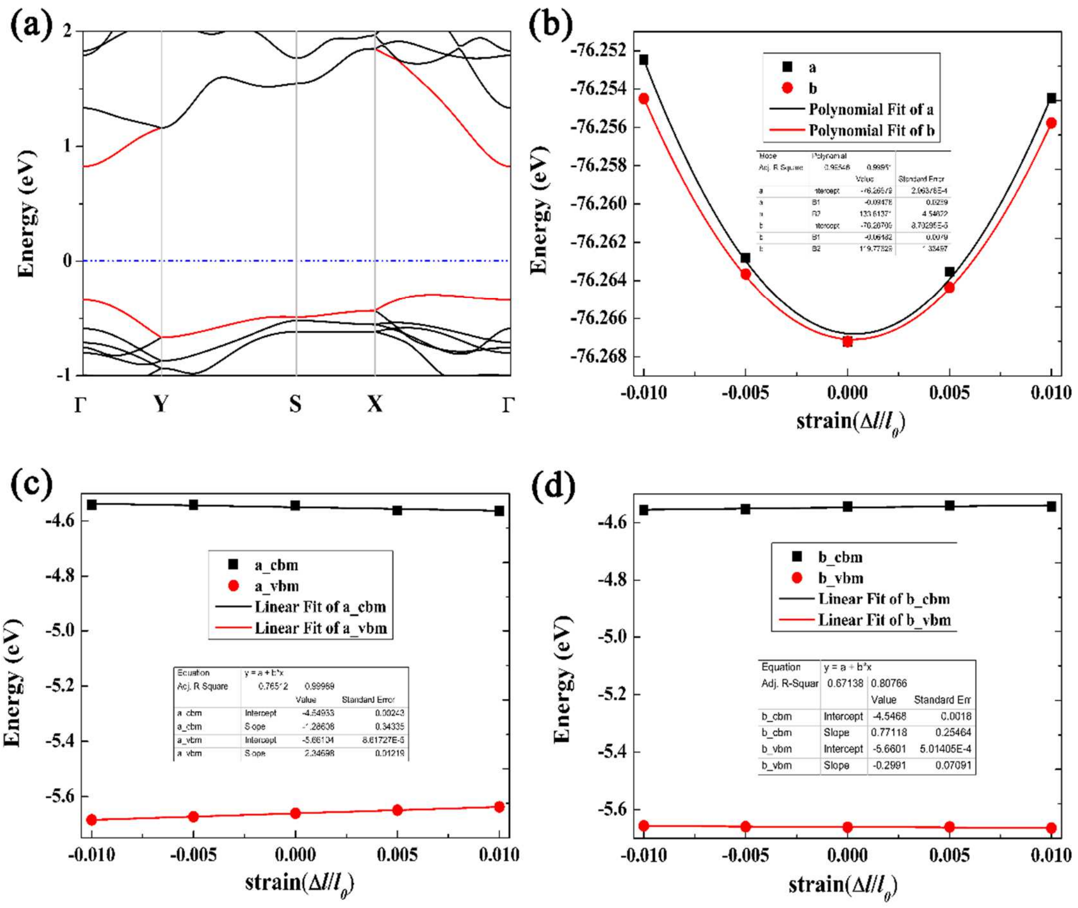

Model	Polynomial		
Adj. R-Square	0.95546	0.9995[illegible]	
		Value	Standard Error
a	Intercept	-76.26679	2.96378E-4
a	B1	-0.09478	0.0259
a	B2	133.61371	4.54672
b	Intercept	-76.26709	8.70295E-5
b	B1	-0.06182	0.0079
b	B2	119.77528	1.33497

Equation	y = a + b*x		
Adj. R Square	0.76512	0.99989	
		Value	Standard Error
a_cbm	Intercept	-4.54933	0.00243
a_cbm	Slope	-1.28608	0.34335
a_vbm	Intercept	-5.66104	8.61727E-5
a_vbm	Slope	2.34698	0.01219

Equation	y = a + b*x		
Adj. R-Squar	0.67138	0.80766	
		Value	Standard Err
b_cbm	Intercept	-4.5468	0.0018
b_cbm	Slope	0.77118	0.25464
b_vbm	Intercept	-5.6601	5.01405E-4
b_vbm	Slope	-0.2991	0.07091

Fig. S4 (a) Electronic band structure of $Ge_2P_4S_2$ monolayer in an orthogonal supercell; (b) Total energy difference between the unstrained and strained $Ge_2P_4S_2$ monolayers along the *a* and *b* directions; (c) Energy shift of VBM and CBM for monolayer $Ge_2P_4S_2$ with respect to the lattice dilation and compression along the *a* direction; (d) Energy shift of VBM and CBM for monolayer $Ge_2P_4S_2$ with respect to the lattice dilation and compression along the *b* direction.

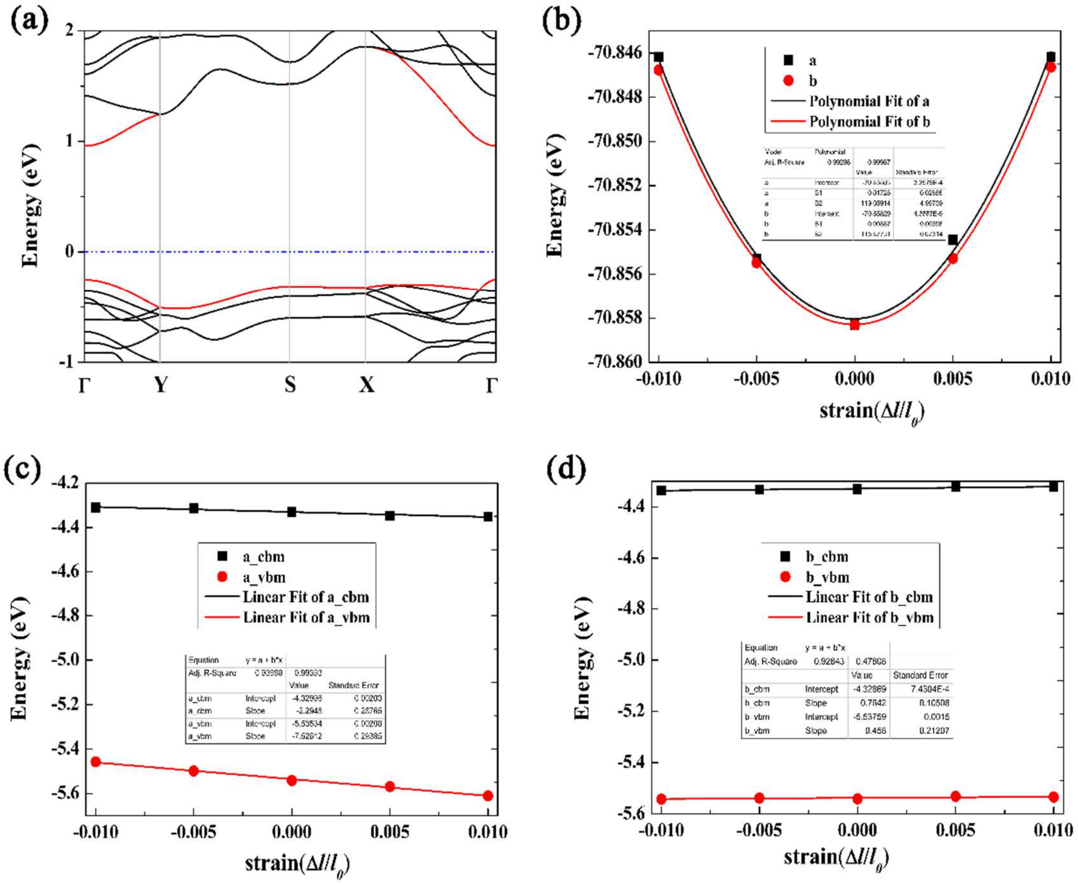

Model	Polynomial		
Adj. R-Square	0.99296	0.99967	
		Value	Standard Error
a	Intercept	-70.85806	3.2579E-4
a	B1	0.01725	0.02566
a	B2	119.05914	4.99759
b	Intercept	-70.85829	4.2883E-5
b	B1	0.00887	0.00358
b	B2	115.67731	0.67314

Equation	y = a + b*x		
Adj. R-Square	0.93998	0.99330	
		Value	Standard Error
a_cbm	Intercept	-4.32998	0.00203
a_cbm	Slope	-2.2948	0.28765
a_vbm	Intercept	-5.53534	0.00208
a_vbm	Slope	-7.52612	0.29385

Equation	y = a + b*x		
Adj. R-Square	0.92843	0.47808	
		Value	Standard Error
b_cbm	Intercept	-4.32869	7.4304E-4
b_cbm	Slope	0.7642	0.10508
b_vbm	Intercept	-5.53759	0.0015
b_vbm	Slope	0.458	0.21207

Fig. S5 (a) Electronic band structure of $Ge_2As_4S_2$ monolayer in an orthogonal supercell; (b) Total energy difference between the unstrained and strained $Ge_2As_4S_2$ monolayers along the *a* and *b* directions; (c) Energy shift of VBM and CBM for monolayer $Ge_2As_4S_2$ with respect to the lattice dilation and compression along the *a* direction; (d) Energy shift of VBM and CBM for monolayer $Ge_2As_4S_2$ with respect to the lattice dilation and compression along the *b* direction.

References

1. O. Beckstein, J. E. Klepeis, G. L. W. Hart and O. Pankratov,First-principles elastic constants and electronic structure ofα－Pt2Siand PtSi. Physical Review B, 2001, 63,doi:10.1103/PhysRevB.63.134112.
2. Y. Chen, Q. Sun and P. Jena,SiTe monolayers: Si-based analogues of phosphorene. Journal of Materials Chemistry C, 2016, 4, 6353-6361,doi:10.1039/c6tc01138a.
3. Y. Wei, Y. Ma, W. Wei, M. Li, B. Huang and Y. Dai,Promising Photocatalysts for Water Splitting in BeN2 and MgN2 Monolayers. The Journal of Physical Chemistry C, 2018, 122, 8102-8108,doi:10.1021/acs.jpcc.8b01081.
4. R. C. Andrew, R. E. Mapasha, A. M. Ukpong and N. Chetty,Mechanical properties of graphene and boronitrene. Physical Review B, 2012, 85,doi:10.1103/PhysRevB.85.125428.
5. Y. Cai, G. Zhang and Y. W. Zhang,Polarity-reversed robust carrier mobility in monolayer MoS(2) nanoribbons. J A*m Chem Soc*， 2014， 136， 6269-6275，doi:10.1021/ja4109787.

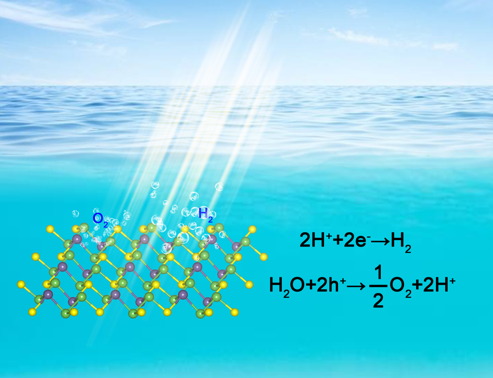

$$2H^+ + 2e^- \rightarrow H_2$$

$$H_2O + 2h^+ \rightarrow \frac{1}{2}O_2 + 2H^+$$